Anuário do Instituto de Geociências
Universidade Federal do Rio de Janeiro
https://revistas.ufrj.br/index.php/aigeo/

ISSN 0101-9759
e-ISSN 1982-3908

Origin and Evolution of the W mineralization in the Intrusion-related Hydrothermal Deposits of the Cerro Áspero Mining District, Sierras Pampeanas, Argentina

Origem e Evolução da Mineralização de W nos Depósitos Hidrotermais relacionados a Rochas Intrusivas do Distrito Mineiro Cerro Áspero, Sierras Pampeanas, Argentina

Sebastián González Chiozza

Universidade Federal do Ceará, Centro de Ciências, Departamento de Geologia, Fortaleza, CE, Brasil
E-mail: sebastian@ufc.br

Abstract

The Cerro Áspero Mining District (CAMD) is located at the Sierras Pampeanas of central Argentina and hosts significant intrusion-related wolframite mineralization. The ore deposits are associated to hydrothermal quartz veins and breccias, hosted by granitoids and metamorphic rocks at the northern contact zone of the Devonian post-orogenic Cerro Áspero Batholith (CAB). The physico-chemical conditions of the different mineralization styles are yet not totally understood, and aiming to deliver a metallogenetic model, the petrography and composition of the main ore and gangue minerals were investigated, and fluid inclusion and stable isotope studies were performed in quartz, muscovite, wolframite, apatite, pyrite, molybdenite, chalcopyrite, and galena. The integrated results revealed that the CAMD ore deposits were generated within the cooling period of the Cerro Áspero Batholith, throughout three late to post-magmatic hydrothermal mineralizing stages. Based on fluid inclusion studies and stable isotope processed data, it was found that the fluids of the first two stages were probably derived from a magmatic source, whereas the third stage solutions would have been originated from meteoric waters. The temperature of the system at the beginning of the hydrothermal phase, was estimated at 384°C; thereafter, the calculated values suggest a decreasing thermal path. Chemical analyses of wolframite showed that the CAMD ore deposit's evolution was signed by initial formation of ferberite, and subsequently evolved with an increasing H/F ratio that conduced to hübnerite precipitation in the final stage.
Keywords: Wolframite; Intrusion-related deposits; Cerro Áspero

Resumo

O Distrito Mineiro Cerro Áspero está situado nas Sierras Pampeanas da Argentina central, e hospeda significativa mineralização de wolframita relacionada a rochas intrusivas. Os depósitos estão associados a veios e brechas de quartzo hidrotermal, hospedadas em granitoides e rochas metamórficas na zona norte do contato do batólito Devoniano pós-orogênico Cerro Áspero. As condições físico-químicas de formação da mineralização do distrito ainda não estão claramente definidas, e no intuito de propor um modelo metalogenético, foram investigadas a petrografia e composição dos principais minerais de minério e ganga, realizando-se também estudos de inclusões fluidas e isótopos estáveis. A integração dos resultados revelou que os depósitos do Distrito Mineiro Cerro Áspero foram gerados durante o período de resfriamento do Batólito Cerro Áspero, através de três estágios mineralizantes tardio a pós-magmáticos. Com base no processamento dos dados de inclusões fluidas e isótopos estáveis, sugere-se que os fluidos dos dois primeiros estágios derivaram de uma fonte magmática, enquanto que as soluções correspondentes ao terceiro estágio teriam sido originadas a partir de águas meteóricas. A temperatura do sistema no início da fase hidrotermal foi estimada em 384ºC; subsequentemente, os valores calculados sugerem um progressivo resfriamento do sistema. As análises químicas realizadas em wolframita mostraram que nos depósitos do distrito, inicialmente, precipitou ferberita, e que a evolução posterior continuou com o incremento do índice H/F levando à formação de hubnerita no estágio final.

Palavras-chave: Wolframita; Depósitos relacionados a rochas intrusivas; Cerro Áspero

1 Introduction

The south-eastern Sierras Pampeanas, considered as a metallogenic province, concentrate most tungsten deposits of the Argentine Republic. Two types of intrusion-related W deposits are common in this province: scheelite skarns (Espeche & Lira, 2019), and magmatic-hydrothermal quartz-wolframite vein systems (Mutti *et al.*, 2005). The Cerro Áspero Mining District (CAMD) belongs to the second type, which is usually connected to post-orogenic granitic intrusions with associated greisen facies.

Since the first documented record of wolframite at the CAMD in the late nineteenth century, its geology has been resumed in different reviews and compilation works (Brodtkorb, 1999; Mutti *et al.*, 2007). Some scientific studies have focused on the petrology (Pinotti *et al.*, 2002) and structural geology of the district (Mutti *et al.*, 2003), and only some specific aspects related to the W hydrothermal deposits have been treated individually (González Chiozza & Mutti, 2002; Mutti & González Chiozza, 2005). Although descriptive information is currently available, there is still the lack of a comprehensive metallogenic study of the CAMD involving physicochemical conditions of formation, fluid and metal sources, chronological and geological relationships. The purpose of this paper is to contribute to fulfill this hiatus by presenting mineral chemistry data and temperature estimations based on fluid inclusions and stable isotopes, in order to develop a consistent metallogenic model for the CAMD.

2 Geological Setting

The Cerro Áspero Mining District (CAMD) integrates the Precambrian-Paleozoic igneous-metamorphic basement of the Comechingones range, being located at the south-eastern Sierras Pampeanas geological province, central Argentina (Figure 1).

During late Proterozoic and early Cambrian times, the Comechingones range area was characterized by a thick volcano-sedimentary marine sequence. Its subsequent evolution, along with the Sierras Pampeanas province, is related to a complex accretionary history that led to the amalgamation of several terrains at the occidental proto-margin of Gondwana through successive eastward subduction-collision episodes (Ramos, 1999).

Initially, the Pampia terrain, where the CAMD is placed, was incorporated to the Río de la Plata craton at ~535 Ma (Pampean orogeny – from Neoproterozoic to early Cambrian). After this episode, accretion along the western margin continued with Cuyania terrain at ~465 Ma (Famatinian orogeny – from late Cambrian to Devonian) and Chilenia terrain at ~ 395 Ma (Achalian orogeny – from Devonian to early Carboniferous) (Figure 1). These three orogenic cycles left their structural and petrologic records in the Comenchingones range, which still continues under the influence of the currently active Andean cycle.

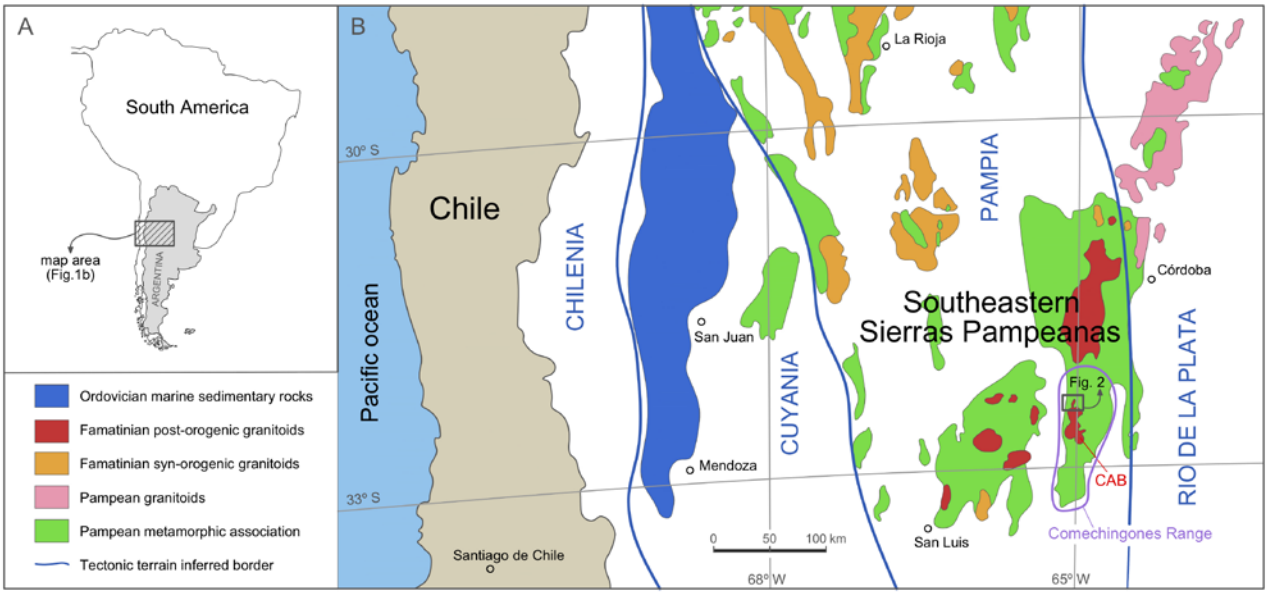

Figure 1 A. Localization map; **B**. Schematic geological map of the central-west Argentina region based on Ramos (1999) and Rapela & Pankhurst (2002).

3 Geology of the CAMD

The geology of the CAMD consists of a Pampean metamorphic association, which is intruded by the Famatinian granitoids that compose the Cerro Áspero Batholith (CAB) (Figure 1). The Pampean metamorphic association is interpreted as a metasedimentary passive margin sequence (Rapela *et al.*, 1998), and consists of schists, gneisses, amphibolites and migmatites exhibiting an eastward increasing medium to high metamorphic grade. These metamorphic rocks have been partially transformed through late-orogenic (Pampean) shearing, into greenschist facies mylonites (retrograde conditions) that constitute the ~N-S trending Guacha Corral Shear Zone (Figure 2) (Pinotti *et al.*, 2006). Tectonometamorphic processes along this regional ductile shear zone involved dynamic retrograde metamorphism with a strong reworking of pre-existing fabrics, and produced a NNW trending mylonitic foliation, dipping at high angle to the east. According to Pinotti *et al.* (2002), at 369 ± 9 Ma (Rb/Sr) the Guacha Corral Shear Zone constituted a weakness zone that favored the post-orogenic intrusion of the CAB at approximately 800ºC of temperature and less than 2 kb of pressure. Two plutonic bodies integrate the CAB totalizing an outcropping area of 440 km^2, but just the northern and latest of them, the Talita Pluton, crops out within the CAMD area. The CAB rocks have monzogranitic to granodioritic modal compositions with peraluminous and high-K calc-alkaline geochemical signatures along with high contents of large-ion lithophile elements (LILE), P, and Ti (Pinotti *et al.*, 2002). Porphyritic facies with microcline phenocrysts, miarolitic cavities, and late aplites and pegmatites are frequent.

3.1 Geology of the Ore Deposits

The W rich magmatic-hydrothermal ore deposits of the CAMD occur at the N and NE contact zones of the CAB and are hosted by granitoids, amphibolites, schists and mylonites (Figure 2). Two different mineralization styles have been recognized: (1) breccia, and (2) veins and veinlets (González Chiozza & Mutti, 2002).

(1) Breccia bodies of irregular shapes are emplaced in metamorphic rocks that overlie covered portions of the CAB. Three breccias have been identified: Cerro Áspero, Fischer and San Virgilio (Figure 2), the latter showing greater dimensions, with approximately 300 m along its major extension. The bodies are fragment-supported, have mosaic and, subordinately, rotational structures, and are composed of ~80% of fragments (granitoid, amphibolite, mylonite, hydrothermal quartz) which are cemented by quartz containing wolframite along with other metalliferous and gangue minerals (Figure 3A).

(2) Veins and veinlets, composed of hydrothermal quartz with main wolframite mineralization are the most widespread deposit type within the district, comprising about 60 % in volume of the total hydrothermal materials. The tabular bodies are 0.5 to 50 cm in width, with longitudinal extensions that range from a few centimeters to several hundreds of meters. Although veins usually occur in sub-

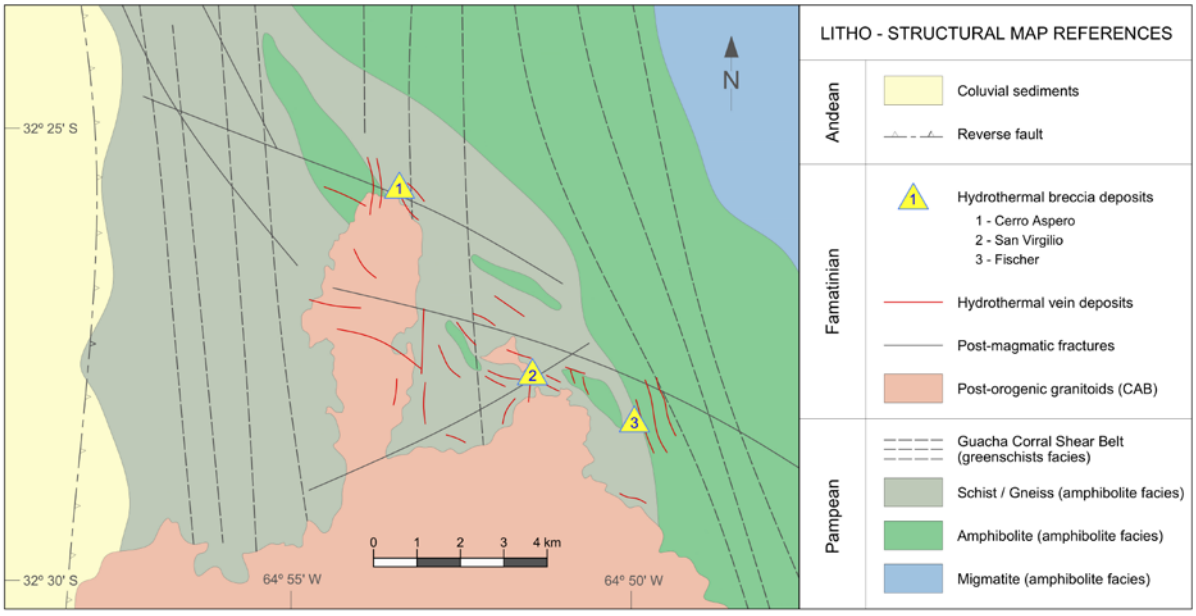

Figure 2 Geological map of the Cerro Áspero Mineralized District based on González Chiozza (2004).

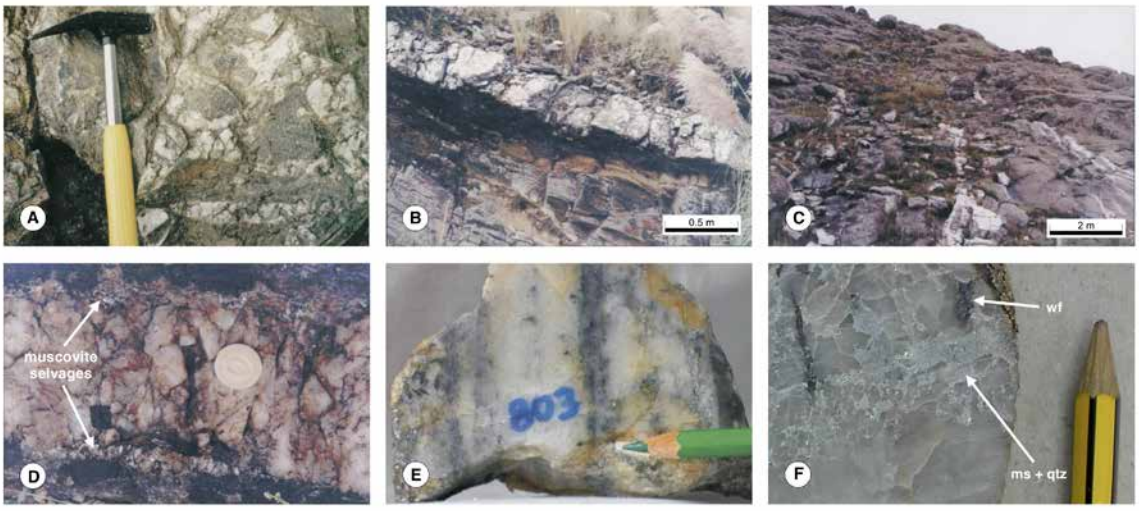

Figure 3 Illustrative photographs of the ore deposits; **A**. Fragment-supported breccia deposit; **B**. Concordant massive hydrothermal vein; **C**. Hydrothermal veins hosted by granite; **D**. Quartz vein with muscovite selvages; **E**. Banded textures with wolframite and sulfides observed in hydrothermal veins; **F**. Veinlets of thin muscovite (ms), quartz (qtz) and wolframite (wf) replacing quartz of previous generation.

vertical position, occasionally they are concordant with the ENE dipping metamorphic foliation (Figure 3B). The veins and veinlets frequently ramify and crosscut one another composing structurally complex swarms of up to 25 m wide (Figure 3C), where stockwork structures are not uncommon. The textures found in vein-type mineralization are massive (Figure 3B and 3D) and banded, frequently revealing superimposition of several crack-seal episodes (Figure 3E). Replacement veinlets consisting of fine-grained aggregates are also common within previous hydrothermal materials (Figure 3F). Wolframite and sulfides are abundant in these veinlets, together with quartz and muscovite as the most typical gangue components.

3.1.1 Chronological Relationships

The age of the mineralization has been determined in 343.8 ± 10.8 Ma through K/Ar dating on muscovite deposited during stage 2 (González Chiozza, 2004). This determination suggests a late to post-magmatic character for the hydrothermal deposits relative to the CAB, which has a Rb/Sr age of 369 ± 9 Ma (Pinotti *et al.*, 2006). Complementary thermal calculations performed by González Chiozza & Mutti (2008), determined that the complete cooling period of the CAB extended for 46.6 Ma. Thus, regarding the CAB emplacement age, it could be considered that the deposit formation occurred within the cooling period of the batholith, which should have ended at approximately 323.3 Ma.

4 Methodology

After field observations and macroscopic inspection, 42 samples were selected out of a wider population, for petrographic investigations. Transmitted and reflected light microscopy was used in polished thin sections and polished buttons, in order to identify the mineral phases and determine the paragenetic relationships. Based on ore petrography, specific samples were prepared for electron microprobe, fluid inclusion, and stable isotope analyses.

4.1 Electron-probe Microanalyses

Mineral compositions were determined on 23 samples through electron-probe microanalyses at the Universidad del País Vasco, Spain, using a Cameca microbeam CMX equipped with TAP, LIF, PET and PC1 analyzing crystals. The analyses were performed with the following configurations: accelerating voltage: 15 – 20 kV, regulated current: 9.1 – 20.3 nA, beam diameter at the emission zone: 2 mm, peak measuring time: 30 seconds, background measuring time: 10 seconds. Samples were previously metalized and SPI STRUCTURE PROBE INC. standards were used for calibration.

4.2 Fluid Inclusions Studies

Fluid inclusions were described according to conventional criteria (Roedder, 1984) and classified

in fluid inclusion assemblages based on petrographic observations. Microthermometric studies were developed at the Universidad del País Vasco, Spain, in 14 doubly-polished ~150mm thick wafers of selected fine to coarse-grained hydrothermal quartz samples. The measurements were carried out with a Chaixmeca heating – freezing stage connected to semi-automatic controllers. The data obtained have a reproducibility of ± 3°C for the heating runs, and ± 1°C for the freezing runs. Salinities (expressed as wt % NaCl eq) are a rough estimate obtained from temperatures of last-ice melting (Bodnar, 1993).

4.3 Stable Isotopes

Stable isotope analyses were carried out on mineral separates (quartz, muscovite, apatite, wolframite, pyrite, chalcopyrite, molybdenite, and galena) and fluid inclusions of the hydrothermal deposits, at the Servicio General de Isótopos Estables, Universidad de Salamanca, Spain. $\delta^{18}O$ was determined on 11 samples, δD on 4 samples, and $\delta^{34}S$ on 4 samples. Oxygen was liberated from minerals through fluorination; then, after purification, it was reduced to CO_2 by reaction with a graphite rod heated by a platinum wire. For hydrogen measurements, water was released, either from minerals or fluid inclusions, by heating under vacuum; extracted water was then reduced to H_2 over U at 750ºC. SO_2 was directly extracted by calcination under vacuum, from powdered sulfide samples added with CuO. Isotopic measurements of CO_2 ($\delta^{18}O$), H_2 (δD) and SO_2 ($\delta^{34}S$) gases were made using VG-Sira II mass spectrometers, with VSMOW standard calibration for $\delta^{18}O$ and δD, and CDT standard calibration for $\delta^{34}S$. Final reported values represent the average of 10 measurements.

5 Results

5.1 Paragenetic Sequence and Mineralogy

The main hydrothermal metallic minerals associated with the quartz-wolframite deposits include molybdenite, tetradymite, wittichenite, pavonite, miharaite, stannoidite, geffroyite, chalcopyrite, pyrite, sphalerite, galena, and altaite. Non-metallic gangue minerals are represented mainly by muscovite, apatite, fluorite, and tourmaline with minor K-feldspar, albite, chlorite, and topaz. Detailed observation of mineral assemblages and their associated ore structures enabled the distinction of three major stages of mineralization throughout the late to post-magmatic hydrothermal phase. Each metalliferous stage represents a discrete mineralizing event that has its distinctive paragenesis and particular structural and textural relationships. The study of these features provided consistent information relative to the deposit formation and is summarized in Figure 4.

5.1.1 Stage 1 (subordinated wolframite – quartz – muscovite)

The stage 1 (S1) deposits consist of veins and veinlets, which are widely distributed throughout the whole district and hold the greatest volumes of hydrothermal minerals. Despite the abundance of hydrothermal quartz, very little amounts of wolframite are found in this stage, which is mainly composed of milky quartz with accessory muscovite and variable presence of tourmaline, fluorite, K-feldspar, and albite. Deposits usually have muscovite selvages and massive, banded, or laminated structures with occasional occurrence of geodes (Figures 3D and 5A).

5.1.2 Stage 2 (main wolframite – quartz – apatite)

Stage 2 (S2) has provided the greatest amounts of wolframite to the system, through the generation of the breccia deposits together with replacement veinlets. The breccia cement is dominated by grey to colorless quartz and also includes muscovite and apatite in significant proportions (Figure 5B and 5C) with minor fluorite, tourmaline, topaz, and chlorite. Wolframite is hosted within these gangue minerals and is frequently associated with pyrite and minor chalcopyrite, sphalerite and molybdenite. Replacement veinlets crosscut the S1 veins and are essentially composed of fine-grained greisen-like aggregates of quartz and muscovite (Figures 3F and 5D), with small amounts of apatite and fluorite. The metallic phases present in these deposits are wolframite, chalcopyrite, molybdenite, and pyrite (Figures 6A and 6B).

5.1.3 Stage 3 (main sulfides – quartz – muscovite)

Stage 3 (S3) produced abundant replacement veinlets through millimetric fractures, affecting previous stages (Figures 5E and 5F). Laminated structures are observed (Figures 3E and 5E), suggesting that multi-episodic deposition took place through fracturing and healing, *i.e.*, crack-and-seal mechanism. The mineral association is dominated by sulfide minerals, namely chalcopyrite, pyrite, molybdenite, sphalerite, galena, tetradymite, pavonite, wittichenite, miharaite, stannoidite, geffroyite, and altaite (Figures 6C, 6D, 6E, and 6F), but also includes wolframite, muscovite, apatite and grey to milky quartz. Minerals appear as fine to medium grains, developing disseminated textures within the fractured S1 and S2 materials.

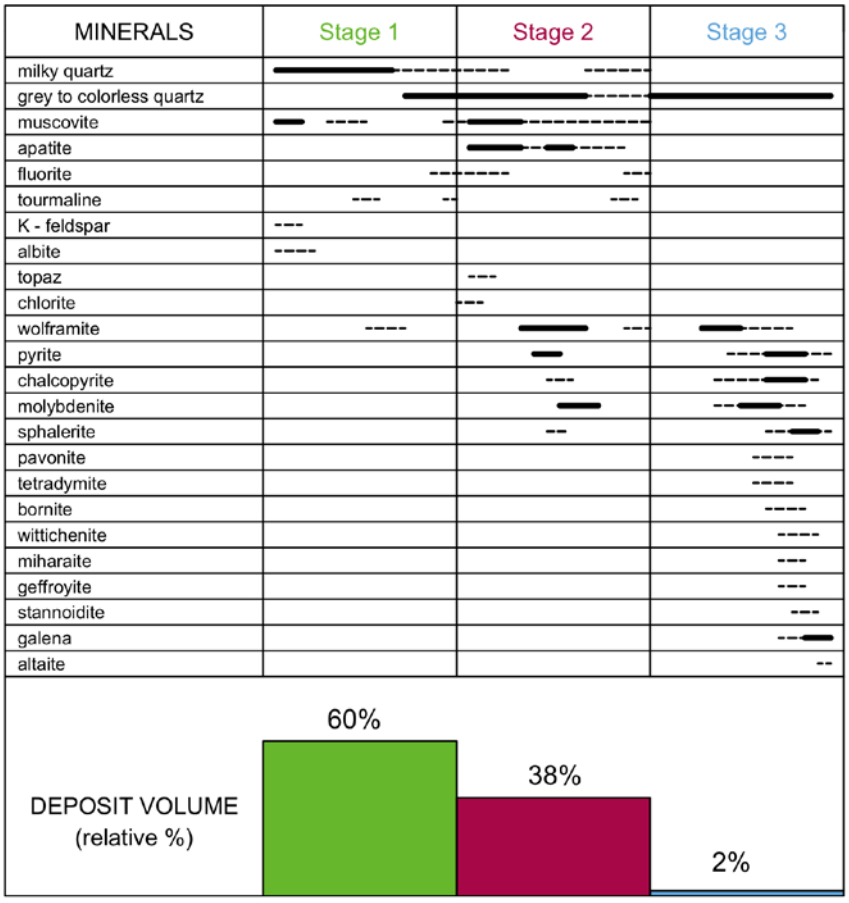

Figure 4 Paragenetic evolution of the hydrothermal mineralizing stages of the CAMD. Full thick line indicates principal components whereas dashed trace is used for accessory minerals.

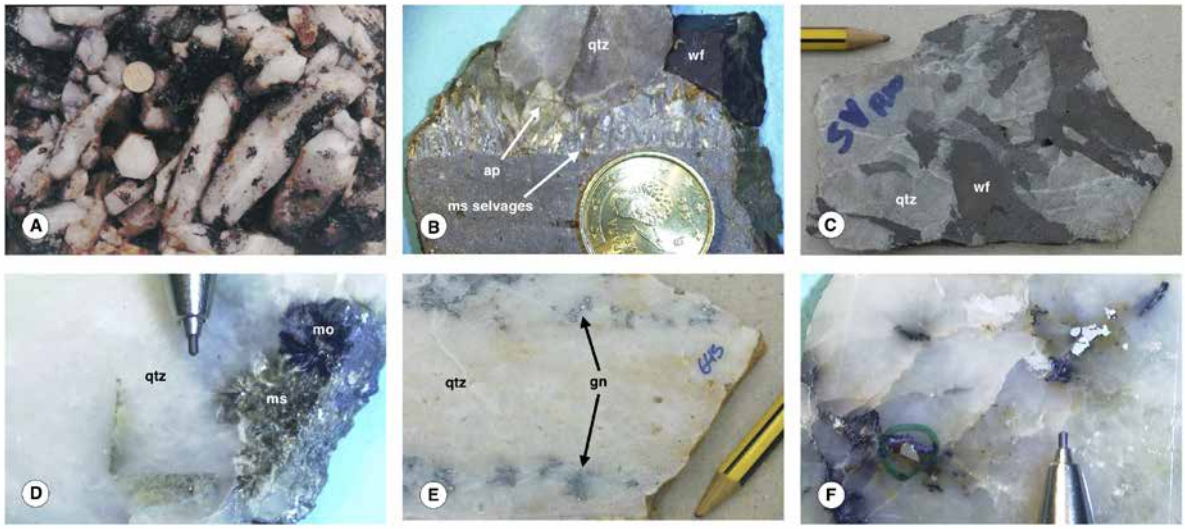

Figure 5 Illustrative photographs of the mineralization; **A**. S1 geodic cavity lined with quartz crystals; **B**. S2 quartz vein with muscovite (ms) selvages, apatite (ap) and wolframite (wf); **C**. S2 large euhedral wolframite (wf) crystals surrounded by grey quartz (qtz); **D**. S1 white quartz (qtz) with S2 replacement veinlets containing muscovite (ms) and molybdenite (mo); **E**. S3 veinlets with galena (gn) replacing S1 quartz (qtz); **F**. S3 sulfide association replacing S1 fractured quartz.

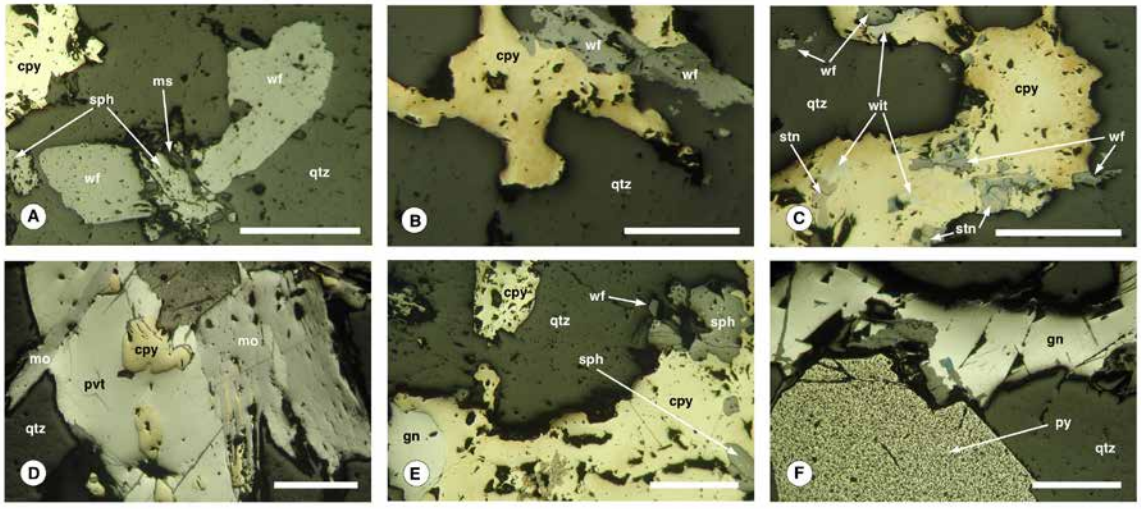

Figure 6 Selected photomicrographs showing paragenetic features from the CAMD quartz (qtz) hosted ore deposits; **A**. S2 mineral association: wolframite (wf) + chalcopyrite (cpy) + sphalerite (sph) with chalcopyrite disease + muscovite (ms); **B**. S2 mineral association: wolframite (wf) + chalcopyrite (cpy); **C**. S3 mineral association: wolframite (wf) + chalcopyrite (cpy) + wittichenite (wit) + stannoidite (stn) with covellite (cv) replacement; **D**. S3 mineral association: chalcopyrite (cpy) + molybdenite (mo) + pavonite (pvt); **E**. S3 mineral association: wolframite (wf) + chalcopyrite (cpy) + galena (gn) + sphalerite (sph) with chalcopyrite disease; **F**. S3 mineral association: galena (gn) + pyrite (py). The white bar is 400 µm long.

5.2 Mineral Chemistry

Selected electron microprobe analyses, which aided the identification of the ore components, are reported in Table 1.

Additionally, specific electron microprobe determinations were carried out in several specimens of wolframite in order to monitor its compositional variation throughout the deposit's evolution (Table 2). The calculated hübnerite/ferberite ratio (H/F), defined as 100 x Mn/(Mn + Fe) (Michaud & Pichavan, 2019), is used as an indicator of the Fe depletion in wolframite.

5.3 Fluid Inclusion Petrography and Microthermometry

Through petrographic analysis, primary and secondary fluid inclusion assemblages were distinguished and classified into three types (I, II and III), which, according to occurrence aspects, could be correlated to the three mineralizing stages (Figure 7). The results obtained after the microthermometric studies of the three fluid inclusion types are summarized in Table 3 and Figure 8.

Type I fluid inclusions are found in S1 quartz crystals exhibiting primary origin features; therefore, it could be assumed that the trapped fluids are samples of the original S1 fluids that deposited the host mineral. Type I includes two-phase aqueous inclusions composed by H_2O (L) + H_2O (V) (Figure 7A). These inclusions, which occur randomly or in small families within coarse-grained quartz, have regular shapes, usually show negative crystal relief, and range in size from 5 to 20 µm. Two coexistent sub-types have been differentiated within the assemblages: a vapor-rich sub-type with ~ 85 vol % of vapor, and a liquid-rich sub-type with 35 – 50 vol % of vapor. The vapor-rich inclusions homogenize to the vapor state, whereas those corresponding to the liquid-rich sub-type homogenize into the liquid state. The average value of –20.7 ºC obtained for the eutectic temperature, suggests that the system was mainly composed of H_2O and NaCl. Nevertheless, some sporadic movements observed in the inclusions between –56.1 and –54 ºC, may indicate minor participation of CO_2.

Type II primary fluid inclusions are widespread within S2 fine-grained quartz samples, suggesting that they bear S2 mineralizing fluids. They occur both as isolated fluid inclusions and in clusters, showing two immiscible liquid phases at room temperature: H_2O (L) + HC (L). Inclusions of this type typically display rounded to polyhedral shapes with a diameter range between 5 and 35 µm. The aqueous phase composes 80 to 95 vol % of these inclusions, while the remnant is occupied by a flattened bubble of a dark grey fluid (Figure 7B). In various cases, a tiny (< 1 µm) solid black particle has been detected within the inclusions. When exposed to thermal changes, the behavior of type II fluid inclusions shows certain singularities that suggest hydrocarbon presence, according to observations made by Burruss (1981): a) when decrepitation of an inclusion occurs, permanent brownish-black splits are produced in and around the inclusion; b) when the fluid inclusion is

Table 1 Microprobe analyses and calculated ion contents of metalliferous minerals corresponding to stage 3. bdl: below detection limit. (*) indicates data after González Chiozza *et al.* (2002).

Mineral	chalcopyrite	geffroyite	wittichenite	wittichenite	tetradimite	galena	pavonite	miharaite	stanoidite	altaite
Fórmula	$FeCuS_2$	$(Ag,Cu,Fe)_9(Se,S)_8$	Cu_3BiS_3	$(Cu,Ag)_3BiS_3$	Bi_2Te_2S	PbS	$(Ag,Cu)(Bi,Pb)_3S_5$	$PbCu_4FeBiS_6$	$Cu_8(Fe,Zn)_3Sn_2S_{12}$	PbTe
Sample	**207 (8)**	**202 (7)**	**225 (15)**	**225 (24)**	**225 (19)**	**202 (7)**	**12 (5)**	**51a (*)**	**51a (*)**	**645 (*)**
Cu	34.57	26.77	40.34	26.77	0.12	bdl	2.32	29.34	39.62	bdl
Fe	30.11	23.54	0.45	0.03	0.01	bdl	0.03	6.08	9.65	bdl
Mn	bdl	bdl	bdl	bdl	bdl	bdl	bdl	bdl	bdl	bdl
Zn	0.05	bdl	bdl	bdl	bdl	0.01	bdl	0.05	3.57	bdl
Pb	bdl	bdl	bdl	bdl	bdl	84.72	2.68	22.38	bdl	63.20
Bi	0.06	0.01	40.45	39.91	58.81	0.00	68.29	20.58	bdl	0.08
Sn	bdl	bdl	bdl	bdl	bdl	bdl	bdl	bdl	17.61	bdl
Ag	bdl	20.96	0.09	16.06	0.00	0.05	7.68	0.27	0.10	0.02
Cd	bdl	bdl	bdl	bdl	bdl	bdl	bdl	bdl	bdl	bdl
Hg	bdl	bdl	bdl	bdl	bdl	bdl	bdl	bdl	bdl	bdl
Sb	bdl	bdl	0.02	0.04	0.20	0.05	bdl	bdl	bdl	bdl
As	0.03	0.01	bdl	bdl	bdl	0.01	bdl	bdl	0.01	bdl
Se	bdl	0.01	0.03	0.08	0.39	0.03	0.08	bdl	bdl	0.04
Te	0.02	0.07	bdl	0.08	36.27	0.01	0.42	bdl	bdl	37.00
S	35.01	29.32	20.55	18.68	4.66	14.05	18.53	21.21	29.11	bdl
total	99.84	100.69	101.93	101.65	100.46	98.94	100.04	99.91	99.67	100.34
Cu	1.00	3.67	3.00	2.19	0.01	0.00	0.32	4.16	8.17	0.00
Fe	0.99	3.67	0.04	0.00	0.00	0.00	0.01	0.98	2.26	0.00
Mn	0.00	0.00	0.00	0.00	0.00	0.00	0.00	0.00	0.00	0.00
Zn	0.00	0.00	0.00	0.00	0.00	0.00	0.00	0.01	0.72	0.00
Pb	0.00	0.00	0.00	0.00	0.00	0.96	0.11	0.97	0.00	1.02
Bi	0.00	0.00	0.92	0.99	1.95	0.00	2.85	0.89	0.00	0.00
Sn	0.00	0.00	0.00	0.00	0.00	0.00	0.00	0.00	1.94	0.00
Ag	0.00	1.69	0.00	0.77	0.00	0.00	0.62	0.02	0.01	0.00
Cd	0.00	0.00	0.00	0.00	0.00	0.00	0.00	0.00	0.00	0.00
Hg	0.00	0.00	0.00	0.00	0.00	0.00	0.00	0.00	0.00	0.00
Sb	0.00	0.00	0.00	0.00	0.01	0.00	0.00	0.00	0.00	0.00
As	0.00	0.00	0.00	0.00	0.00	0.00	0.00	0.00	0.00	0.00
Se	0.00	0.00	0.00	0.00	0.03	0.00	0.01	0.00	0.00	0.00
Te	0.00	0.00	0.00	0.00	1.97	0.00	0.03	0.00	0.00	0.97
S	2.01	7.96	3.03	3.03	1.01	1.03	5.05	5.96	11.89	0.00
total ions	4.00	17.00	7.00	7.00	5.00	2.00	9.00	13.00	25.00	2.00

frozen, a thin dark film is formed at some section of the wall; c) different phases of the inclusion show relative relief variations as temperature changes; d) no change has been experienced by the solid black particle, neither at high temperatures (~500 ºC) nor at low ones (~ –140 ºC).

Type III fluid inclusion assemblages occur in trails associated with healed fracture planes within S1 and S2 quartz crystals. As these inclusions exhibit secondary origin features while being hosted in S1 and S2 quartz crystals, they are considered to be representative of S3 hydrothermal fluids, which would have circulated through the fractured materials of the previous stages. This type consists of two-phase aqueous inclusions composed by H_2O (L) + H_2O (V). They are irregularly shaped with occasional development of planar faces, showing longitudinal extensions that range between 5 and 30 μm, and vapor bubble occupying 10 –

Table 2 Representative electron microprobe analyses and mineral formula calculations for wolframite specimens of stages 1, 2 and 3. Based on the hübnerite/ferberite ratio (H/F), the minimum (Min), maximum (Max) and average (Avg) compositions are indicated for each stage. bdl: below detection limit.

Stage		**S1**			**S2**			**S3**	
Sample	Min	Max	Avg (9)	Min	Max	Avg (46)	Min	Max	Avg (20)
SiO_2	bdl	bdl	bdl	bdl	bdl	bdl	bdl	bdl	bdl
WO_3	75.13	74.01	74.69	76.60	74.89	75.93	75.53	75.83	75.35
FeO	17.45	13.11	14.99	16.48	5.75	10.62	8.68	3.11	4.29
MnO	5.68	11.17	8.71	7.26	18.36	12.86	14.34	20.18	19.27
MgO	0.22	0.03	0.10	0.13	bdl	0.05	bdl	0.02	0.01
CaO	0.05	0.03	0.02	bdl	bdl	0.03	0.02	0.01	0.01
ZnO	0.05	0.04	0.05	bdl	bdl	0.03	0.06	bdl	0.05
Cu_2O	0.06	bdl	0.03	bdl	bdl	0.05	0.10	0.08	0.03
Total	98.48	98.39	98.59	100.47	99.00	97.42	98.72	99.22	99.00
Cations in formula calculations based on 4 oxygen anions									
W	1.00	0.98	0.99	1.00	0.98	0.99	1.00	1.00	0.99
Fe^{2+}	0.75	0.56	0.64	0.69	0.24	0.45	0.37	0.13	0.18
Mn	0.25	0.48	0.38	0.31	0.78	0.55	0.62	0.87	0.83
Mg	0.02	0.00	0.01	0.01	0.00	0.00	0.00	0.00	0.00
Ca	0.00	0.00	0.00	0.00	0.00	0.00	0.00	0.00	0.00
Zn	0.00	0.00	0.00	0.00	0.00	0.00	0.00	0.00	0.00
Cu	0.00	0.00	0.00	0.00	0.00	0.00	0.00	0.00	0.00
O	4.00	4.00	4.00	4.00	4.00	4.00	4.00	4.00	4.00
H/F	24.78	46.32	36.94	30.86	76.38	55.03	62.58	86.81	81.94

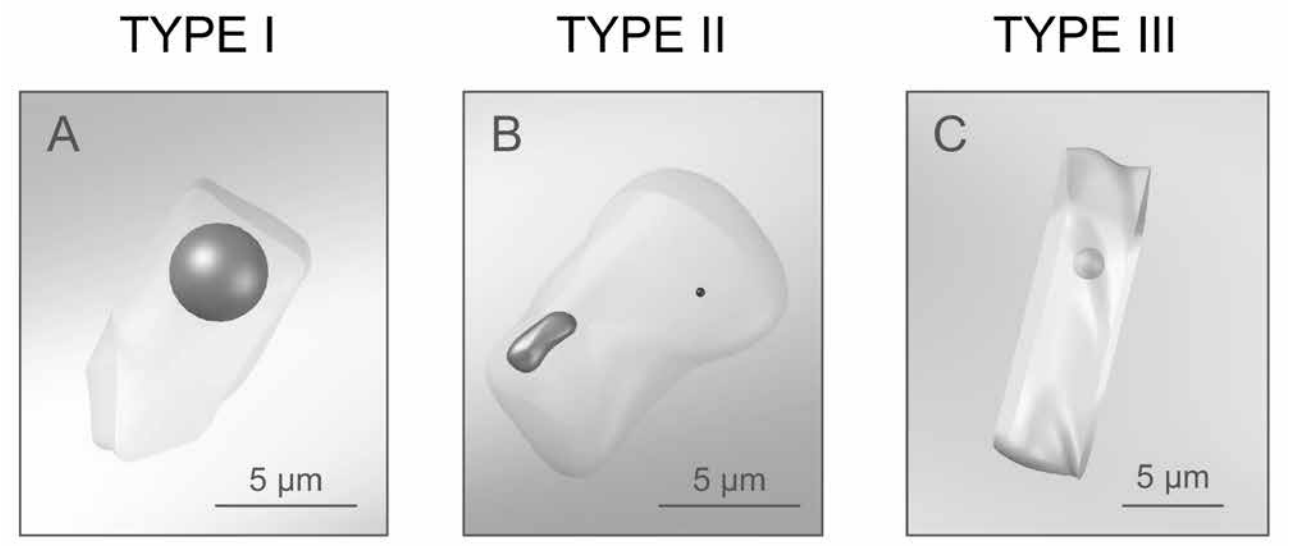

Figure 7 Schematic illustrations of the three fluid inclusion types identified for the CAMD hydrothermal deposits; **A**. Type I inclusions bearing S1 fluids; **B**. Type II inclusions bearing S2 fluids; **C**. Type III inclusions bearing S3 fluids.

Table 3 Summarized fluid inclusion data reporting average values for final ice melting temperature (Tm), homogenization temperature (Th), salinity (NaCl eq) and density (ρ). Number of measurements indicated in parentheses.

Type	Stage	Phases	Tm (°C)	Th (°C)	NaCl eq (wt %)	ρ (g cm^{-3})
I	S1	H_2O_{liq} + H_2O_{vap}	-4.3 (32)	384 (71)	6.8	0.61
II	S2	H_2O_{liq} + HCl_{liq}	-3.3 (11)	279 (23)	5.4	0.81
III	S3	H_2O_{liq} + H_2O_{vap}	-5.3 (15)	226 (27)	8.2	0.91

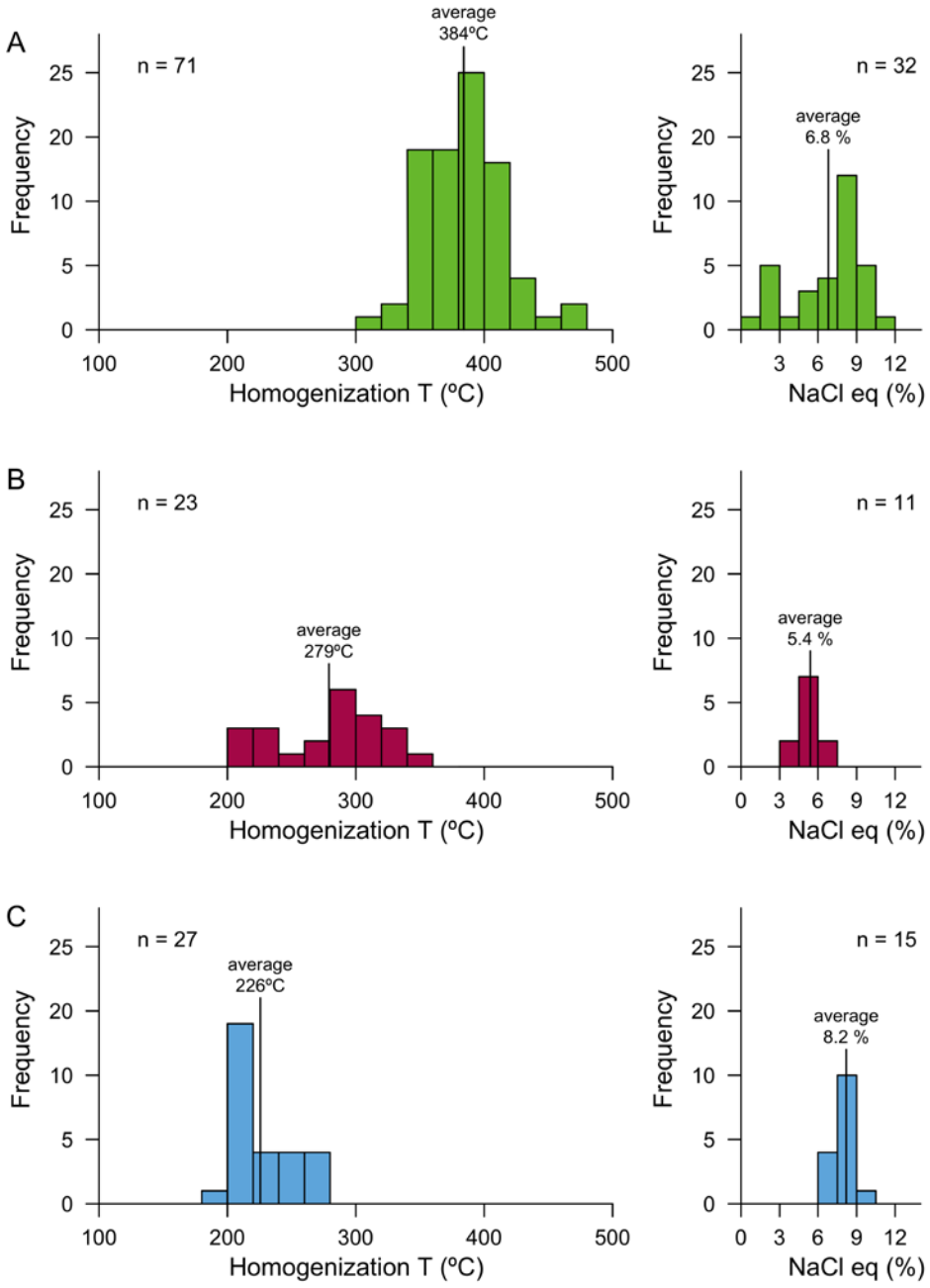

Figure 8 Fluid inclusion histograms representing homogenization temperatures (Th) and salinities (NaCl eq) for the hydrothermal mineralizing fluids of the CAMD; **A**. Type I inclusions bearing S1 fluids; **B**. Type II inclusions bearing S2 fluids; **C**. Type III inclusions bearing S3 fluids.

20 vol % of the inclusion (Figure 7C). A eutectic mean temperature of –19.5 ºC, suggests that the aqueous phase contains dissolved NaCl.

5.4 Stable Isotopes

The $\delta^{18}O$, δD and $\delta^{34}S$ values of quartz, muscovite, apatite, wolframite, pyrite, molybdenite, chalcopyrite, galena and fluid inclusions from CAMD deposits (S1, S2 and S3) are presented in Table 4. Isotope geothermometry and isotope composition of fluids based on this data, will be further presented (see sections 6.1.2 and 6.2).

6 Data Processing and Discussion

6.1 Geothermometry

Temperatures of deposit formation were estimated through different methods, which were selected according to the specific conditions of each mineralizing stage and data availability. For the first stage, fluid inclusion studies suggest boiling conditions and therefore, provide the temperature of formation. In the case of the second stage, available isotopic data allow the use of isotope geothermometry, which provides a more accurate temperature value than the minimum temperature obtained through fluid inclusions. For the third stage, due to the lack of other reliable analytical data, the minimum temperature value obtained through fluid inclusion studies has been considered. A reference temperature value, needed to develop fluid isotopic composition calculations, has been determined for each stage.

6.1.1 Fluid Inclusion Geothermometry

According to Roedder & Bodnar (1980), a boiling liquid and its coexisting vapor phase can be trapped separately in liquid and vapor inclusions respectively. On cooling, both types of inclusions will become two-phase (liquid + vapor): while the liquid inclusions develop a vapor bubble due to liquid contraction, the vapor inclusions develop a film of liquid by condensation. On reheating (during microthermometric studies), homogenization must occur in both cases at the same temperature, which theoretically represents the original temperature of trapping. The coexistence of liquid-rich and vapor-rich aqueous fluid inclusions within type I (S1) inclusions, as well as their almost coincident Th ranges (313-469ºC and 336-410ºC, respectively), suggest that the hydrothermal solutions that originated S1 deposits were at boiling conditions (at least locally) when mineral deposition took place. This fact indicates that the temperature and pressure of homogenization are equivalent to temperature and pressure of formation. Therefore, the average value of 384°C will be considered as a reference temperature of formation for S1 (Figure 8).

Table 4 Stable isotope results obtained for samples of the CAMD. FI: fluid inclusion.

Sample	Mineral	Stage	$\delta^{18}O$	δD	$\delta^{34}S$
SVa	quartz	1	12.3	–	–
SVa	wolframite	1	5.6	–	–
SVa	FI	1	–	–82.4	–
17a	FI	1	–	–68.9	–
51a	quartz	1	12.3	–	–
51b	apatite	2	8.8	–	–
51b	apatite	2	8.4	–	–
92c	quartz	2	12.9	–	–
92c	quartz	2	13.0	–	–
92c	muscovite	2	9.5	–103.4	–
SVa	quartz	2	13.4	–	–
SVa	wolframite	2	4.9	–	–
SVa	muscovite	2	9.1	–125.4	–
22	pyrite	2	–	–	4.7
23	molybdenite	2	–	–	4.8
51c	chalcopyrite	3	–	–	6.0
645	galena	3	–	–	3.1

In the case of S3, as no constraints for maximum temperature could be defined, the average homogenization temperature of 226 ºC could be considered as the minimum temperature of formation (Figure 8).

6.1.2 Isotope Geothermometry

The methodology presented by Campbell & Larson (1998), which assumes that minerals in equilibrium were deposited by the same fluid and at the same temperature, was employed to estimate the temperature of S2 fluids. $\delta^{18}O$ values determined for quartz, muscovite and wolframite, which compose a S2 equilibrated mineral assemblage (Figure 5B) were used to develop geothermometric calculations. Considering each possible combination between the three minerals in equilibrium, three fractionation equations were obtained by subtracting the individual mineral – water fractionation equations. The results obtained separately with the three pairs are quite consistent, ranging between 330.2 and 347.5°C (Table 5). It shall be observed that this range is in agreement with the fluid inclusion average homogenization temperature of 279 ºC, which should be considered as a minimum temperature. The average value of 338°C will be used for fluid isotopic composition calculations (section 6.2) as a reference temperature of formation for S2.

6.2 Isotopic Composition of the Mineralizing Fluids

Tables 6, 7, and 8 summarize the oxygen, hydrogen and sulfur isotopic data, including the calculated isotopic signature of the fluids in equilibrium with the analyzed minerals and the considered temperatures. In cases where fluids were directly extracted from fluid inclusions, a rough estimative composition of the parent fluid composition was obtained after direct measurement.

Calculated $\delta^{18}O_{fluid}$ contents for stage 1 hydrothermal fluids range between 7.3 and 8.3 ‰; whereas δD_{fluid} values measured directly from primary fluid inclusions of the same stage are between –82.4 and –68.9 ‰ (Tables 6 and 7). As shown in Figure 9A, the set of values corresponding to this stage is wholly included within the magmatic field, strongly suggesting that the origin of these fluids was derived from the CAB magmatic activity. Fluid composition calculations performed for stage 2 resulted in $\delta^{18}O_{fluid}$ values ranging from 7.0 to 7.4 ‰ and δD_{fluid} values between –89.6 and –66.7 ‰

Table 5 Isotope geothermometry calculations for the three mineral pairs of the equilibrium assemblage. Mineral – water fractionation equations considered for quartz, muscovite and wolframite after Zhang *et al.* (1989), Bottinga & Javoy (1973), and Zhang *et al.* (1994), respectively.

Mineral phases		Equation	α_{x-y}	Temperature (ºC)
x	y			
quartz	wolframite	$10^3 \ln\delta_{x-y} = 0.176*(10^6/T^2) + 6.42*(10^3/T) - 2.59$	1.0085	336.0
quartz	muscovite	$10^3 \ln\delta_{x-y} = 1.406*(10^6/T^2) + 0.39$	1.0043	330.2
wolframite	muscovite	$10^3 \ln\delta_{x-y} = 1.23(10^6/T^2) - 6.42*(10^3/T) + 2.98$	1.0085	347.5

Table 6 $\delta^{18}O$ (‰) values measured in minerals and $\delta^{18}O$ (‰) values calculated for the parental mineralizing fluids with the referenced fractionation equations.

Mineral	$10^3 \cdot \ln(\alpha_{min-H2O})$ equation	sample	stage	$\delta^{18}O_{min}$	T(°C)	$\delta^{18}O_{fluid}$
quartz	$= 3{,}306(10^6/T^2) - 2{,}71$ Zhang *et al.* (1989)	51a	1	12,3	384	7,3
		SVa	1	12,3	384	7,3
		92c	2	12,9	338	7,2
		92c	2	13,0	338	7,3
		SV	2	13,4	338	7,2
muscovite	$= 1{,}90(10^6/T^2) - 3{,}10$ Botinga & Javoy (1973)	92c	2	9,5	338	7,0
		SV	2	9,1	338	7,1
wolframite	$= 3{,}13(10^6/T^2) - 6{,}42(10^3/T) - 0{,}12$ Zhang *et al.* (1994)	SV	2	4,9	338	7,2
		SVa	1	5,6	384	8,3
apatite	$= 3{,}81(10^6/T^2) - 6{,}63(10^3/T) + 2{,}08$ Zheng (1996)	51a	2	8,8	338	7,4
		51a	2	8,4	338	7,0

(Tables 6 and 7). This isotopic signature overlaps, in part, stage 1 values and it is mostly included within the magmatic field (Figure 9A). Although these features indicate that stage 2 fluids were presumably derived from a magmatic source, the slight deviation from the magmatic field may have been caused by a minor incorporation of connate or meteoric waters. Additionally, the two calculations performed for $\delta^{34}S_{fluid}$ show the same value of 3.6 ‰ (Table 8 and Figure 9B), and support a magmatic derivation for the S2 fluids, as they are situated within the accepted range for magmatic derived sulfur (Campbell & Larson, 1998). $\delta^{34}S_{fluid}$ contents of 5.6 and 6.2 ‰ obtained for stage 3, are considerably higher than the values of stage 2, and exceed the normal values for magmatic sulfur (Figure 9B). Taking into consideration that the metasedimentary country rocks of the area have a marine protolith (Rapela *et al.*,1998) and that $\delta^{34}S_{fluid}$ contents of marine sulfates during the Paleozoic were relatively high: 10 to 30 ‰ (Claypool *et al.*, 1980);

Table 7 δD (‰) values measured in minerals and fluid inclusions and δD (‰) values obtained for the parental mineralizing fluids with the referenced fractionation equations.

mineral	$10^3 \cdot \ln(\alpha_{min-H2O})$ equation	sample	stage	δD_{min}	T(°C)	δD_{fluid}
muscovite	= -22,1($10^6/T^2$) + 19,1 Suzuoki & Epstein (1976)	92c	2	-103,4	338	-66,7
		SV	2	-125,4	338	-89,6
Fluid Inclusions		17a	1	-68,9	384	-68,9
		SVa	1	-82,4	384	-82,4

Table 8 $\delta^{34}S$ (‰) values measured in minerals and $\delta^{34}S$ (‰) values calculated for the parental mineralizing fluids. Fractionation equations after Ohmoto & Rye (1979).

mineral	$10^3 \cdot \ln(\alpha_{min-H2S})$ equation	sample	stage	$\delta^{34}S_{min}$	T(°C)	$\delta^{34}S_{fluid}$
pyrite	= 0,4·($10^6/T^2$)	22	2	4,7	338	3,6
molybdenite	= 0,45·($10^6/T^2$)	23	2	4,8	338	3,6
chalcopyrite	= -0,05·($10^6/T^2$)	51	3	6,0	226	6,2
galena	= -0,63·($10^6/T^2$)	645	3	3,1	226	5,6

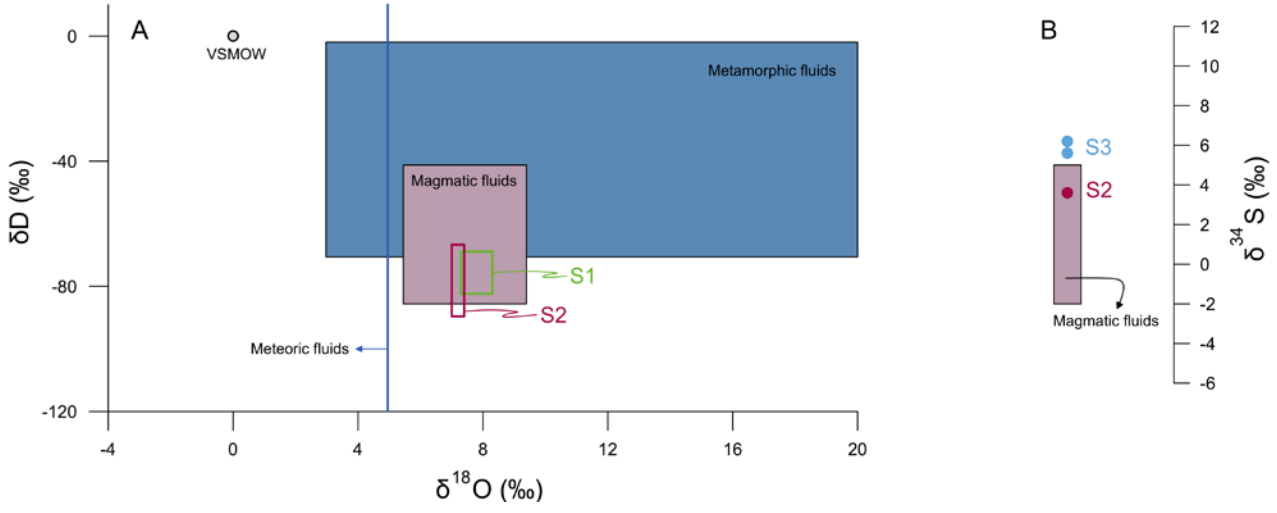

Figure 9 Stable isotope diagrams; A. $\delta^{18}O$ - δD showing the isotopic ranges corresponding to stages 1 and 2; for comparative purposes, the magmatic fluids field after Campbell & Larson (1998), the metamorphic fluids field after Sheppard (1986), the meteoric fluids $\delta^{18}O$ maximum line (Campbell & Larson,1998) and the VSMOW composition have been included; B. $\delta^{34}S$ values for S2 and S3 compared with the magmatic fluids range reported by Campbell & Larson (1998).

it is possible to explain the $\delta^{34}S_{fluid}$ enrichment of stage 3 by the incorporation of crustal sulfur to the fluids through lixiviation processes.

6.3 Evolution of the Deposit Formation

The spatial arrangement of the deposits and the paragenetic and structural relationships between the ore components, indicate that at least three mineralizing stages were involved in the ore deposit formation. According to the stable isotope values, the fluids of the first two stages (S1 and S2) would have derived from a magmatic source (the CAB), whereas the S3 non-magmatic solutions would have evolved from other fluids present in the crust, such as metamorphic, connate and/or meteoric waters.

Temperature estimates suggest that the hydrothermal system's evolution followed a thermal decreasing path, as revealed by the values obtained for S1 (384°C), S2 (330.2 – 347.5°C), and S3 (>226°C).

According to field observations, the S1 produced around 60% of the volume of hydrothermal rocks in the form of veins and veinlets, composed by large amounts of quartz with scarce metals, mainly W, Fe, and Mn (Figure 4). During S2, the magmatic signature of the fluids was still dominant, although lower δD_{fluid} values may reflect an incipient incorporation of meteoric water. Metalliferous supply throughout this stage was markedly increased and included W, Fe, Mn and small amounts of Cu, and Mo, as evidenced by the presence of wolframite, chalcopyrite, molybdenite, and pyrite. Veinlets exhibiting replacement features and fragment-supported breccia bodies with the highest ore contents were generated. Through S2, the mineral deposition was controlled by temperatures around 338°C. Fluid inclusions of this stage appear to contain hydrocarbon components, which are not incompatible with S-type granitoid derived fluids, considering that the magma may have incorporated crustal organic matter from the metasedimentary country rocks during the anatectic melting process. At S3, significant amounts of meteoric water were apparently introduced into the hydrothermal system. Due to the advance in the cooling process and the non-magmatic source, the late S3 mineralizing fluids would have been at lower temperatures than the previous stages. Powered by the intrusive body still acting as a thermal source, the S3 non magmatic solutions circulated and lixiviated the country rocks and the ore deposits of previous generation, incorporating sulfur and metals, as indicated by the $\delta^{34}S$ values. This process introduced a wide diversification in the metallic components (W, Fe, Mn, Mo, Bi, Cu, Zn, Pb, Sn, and Ag), which were deposited in sparse sulfide-rich veinlets at an estimated temperature above 226°C.

At the CAMD, wolframite chemistry showed that the hübnerite/ferberite ratio becomes higher with the progression of the deposit formation (Table 2). It could be considered that initial Fe rich wolframite deposition occurred as a consequence of Fe being less incompatible than Mn. Progressively, ferberite crystallization would have depleted the fluid in Fe and consequently, precipitation of wolframite with higher H/F (hübnerite/ferberite) ratios would have occurred at the advanced stages. Recently, Michaud & Pichavant (2019) proposed that at W deposition environments controlled by ore fluids derived directly from highly evolved granitic magmas, Mn-rich wolframite is characteristic. Nevertheless, the low H/F ratios of the S1 wolframites from CAMD show that magmatic derived hydrothermal brines may also produce Fe-rich wolframite (ferberite) within intrusion-related W deposits, suggesting that a wider range of compositions is possible for this type of deposit.

7 Conclusion

The W intrusion-related hydrothermal ore deposits of the Cerro Áspero Mining District were generated within the cooling period of the Cerro Áspero Batholith, throughout three late to post-magmatic hydrothermal mineralizing stages. The fluids of the first two stages were derived from the late magmatic fluids of the CAB; being the second stage remarkably the main wolframite producer. It is proposed that the third stage solutions would have incorporated meteoric waters and lixiviated sulfur and metals from the country rocks to produce widespread replacement sulfide deposits with diversified mineralogy. Geochemical studies revealed that the earlier ore fluids that were directly derived from the magmatic source produced Fe rich wolframite (ferberite) and that, with decreasing temperature, the H/F ratio progressively augmented.

8 Acknowledgements

This research was supported by the Universidad de Buenos Aires [Projects UBACYT X068 and X138]. The author would like to thank Clemente Recio, Diana Mutti, Fernando Tornos Arroyo, and Francisco Velasco, for all their support during the execution of analytical studies and data processing, as well as Stefanny Matos and the anonymous reviewers of this paper, for their useful comments and suggestions.

9 References

Bodnar, R.J. 1993. Revised equation and table for determining the freezing point depression of H2O NaCl solutions. *Geochimica et Cosmochimica Acta, 57*: 683-684. https://www.sciencedirect.com/science/article/pii/001670379390378A

Bottinga, Y. & Javoy, M. 1973. Comments on oxygen isotope geothermometry. *Earth Planetary Science Letters, 20(2)*: 250-265. https://www.sciencedirect.com/science/article/pii/0012821X73901659

Brodtkorb, M.K. 1999. El distrito wolframífero Cerro Áspero, Córdoba. *In:* ZAPPETTINI, E.O. (Ed.). Recursos Minerales de la República Argentina. Servicio Geológico Minero Argentino, Instituto de Geología y Recursos Minerales. *Anales, 35*: 581-583.

Burruss, R.C. 1981. Hydrocarbon fluid inclusions in studies of sedimentary diagenesis. *In:* HOLLISTER, L.S. & CRAWFORD, M.L. (Eds.). Short course in IF: applications to petrology. Mineralogical Association of Canada, 304 p.

Campbell, A.R. & Larson, P.B. 1998. Introduction to stable isotope applications in hydrothermal systems. *In:* RICHARDS, J.P. & LARSON, P.B. (Eds.). Techniques in hydrothermal ore deposits geology. *Reviews in Economic Geology, 10*: 173-193.

Claypool, G.E.; Holser, W.T.; Kaplan, I.R.; Sakai, H. & Zak, I. 1980. The age curves of sulfur and oxygen isotopes in marine sulfate and their mutual interpretation. *Chemical Geology, 28*: 199-260. https://www.sciencedirect.com/science/article/pii/0009254180900479

Espeche, M.J. & Lira, L. 2019. El origen del wolframio en los depósitos de scheelita de las Sierras Pampeanas de Córdoba: ¿estratoligado o magmático? XIII Congreso de Mineralogía, Petrología Ígnea y Metamórfica, y Metalogénesis, Córdoba. Actas: 298-299.

González Chiozza, S. 2004. Geología y metalogenia del Distrito Minero Cerro Áspero, Sierras Pampeanas de Córdoba, Argentina. Universidad de Buenos Aires, PhD Thesis, 148p.

González Chiozza, S. & Mutti, D.I. 2002. Depósitos mesotermales y Zonación del Distrito Minero Cerro Áspero, Sierras Pampeanas de Córdoba. 15° Congreso Geológico Argentino, Calafate. Actas, 2: 294-499.

González Chiozza, S. & Mutti, D.I. 2008. Estimativa do tempo de esfriamento do Batolito Cerro Áspero (BCA) e sua relação cronológica com a formação dos jazimentos magmático-hidrotermais associados. 44º Congresso Brasileiro de Geologia, Curitiba. Atas: 876.

González Chiozza, S.; Wiechowski, A. & Brodtkorb, M. 2002. Determinaciones mineralógicas en la fase de sulfuros del Distrito Minero Cerro Áspero, Sierras Pampeanas de Córdoba. 6° Reunión de Mineralogía y Metalogenia, Buenos Aires. Actas: 169-172.

Michaud, J.A.S. & Pichavant, M. 2019. The H/F ratio as an indicator of contrasted wolframite deposition mechanisms. *Ore Geology Reviews, 104*: 266–272.

Mutti, D.I.; Tourn, S.M.; González Chiozza, S. & Herrmann, C.J. 2003 Importance of late Famatinian deformation in the exploration for wolfram deposits in Sierras de Córdoba, Argentina. *In:* ELIOPOULOS, D. (Ed.). Mineral Exploration and Sustainable Development. Balkema, Rotterdam, p. 795-798.

Mutti, D.I. & González Chiozza, S. 2005. Evolución petrotectónica del distrito minero Cerro Áspero y modelo de emplazamiento de los depósitos wolframíferos; Córdoba, Argentina. *Revista de la Asociación Geológica Argentina, 60(1)*: 104-121. http://www.scielo.org.ar/scielo.php?script=sci_arttext&pid=S0004-48222005000100015&lng=es&nrm=iso&tlng=es

Mutti, D.I.; Tourn, S.; Caccaglio, O.; Herrmann, C.J.; Geuna, S.E.; Di Marco, A. & Gonzalez Chiozza, S. 2005. Evolución metalogenética de las Sierras Pampeanas de Córdoba y sur de Santiago del Estero: Ciclos famatiniano, gondwánico y ándico. *Revista de la Asociación Geológica Argentina, 60(3)*: 467-485. http://www.scielo.org.ar/scielo.php?script=sci_arttext&pid=S0004-48222005000300004&lng=es&nrm=iso&tlng=es

Mutti, D.I.; Di Marco, A.; Geuna, S.A. & Caccaglio, O. 2007. Depósitos polimetálicos en el orógeno famatiniano de las Sierras Pampeanas de San Luis y Córdoba: fluidos, fuentes y modelo de emplazamiento. *Revista de la Asociación Geológica Argentina, 62(1)*: 44-61. http://www.scielo.org.ar/scielo.php?script=sci_arttext&pid=S0004-48222007000100006&lng=es&nrm=iso&tlng=es

Ohmoto, H. & Rye, R.O. 1979. Isotopes of sulphur and carbon. *In:* H.L. BARNES (Ed). Geochemitry of hydrothermal ore deposits. Wiley and Sons, New York, p. 509-567.

Pinotti, L.; Coniglio, J.; Esparza, A.; D'Eramo, F. & Llambías, E. 2002. Nearly circular plutons emplaced by stoping at shallow crustal levels, Cerro Áspero batholith, Sierras Pampeanas de Córdoba, Argentina. *Journal of South American Earth Sciences, 15*: 251-265. 10.1016/S0895-9811(02)00033-0

Pinotti, L.; Tubía, J.M.; D'Eramo, F.; Vegas, N.; Sato, A.M.; Coniglio, J. & Aranguren, A. 2006. Structural interplay between plutons during the construction of a batholith (Cerro Aspero batholith, Sierras de Córdoba, Argentina). *Journal of Structural Geology, 28*: 834-849. https://doi.org/10.1016/j.jsg.2006.02.004

Ramos, V. 1999. Evolución tectónica de la Argentina. *In:* CAMINOS, R. (Ed.). Geología Argentina. Servicio Geológico Minero Argentino, Instituto de Geología y Recursos Minerales. *Anales, 29*: 715-759.

Rapela, C.W.; Pankhurst, R.J.; Casquet, C.; Baldo, E.; Saavedra, J.; Galindo, C. & Fanning, C.M. 1998. The Pampean Orogeny of the souhern proto-Andes: Cambrian continental collision in the Sierras de Córdoba. *In:* PANKHURST, R. J. & RAPELA, C. W. (Eds.). The Proto-Andean Margin of Gondwana. *Geological Society of London, Special Publications, 142*: 181-217.

Rapela, C.W. & Pankhurst, R.J. 2002. Eventos tecto-magmáticos del Paleozoico inferior en el margen proto-Atlántico del sur de Sudamérica. 15° Congreso Geológico Argentino, Calafate. Actas, 1: 24-29.

Roedder, E. 1984. Fluid Inclusions. *Reviews in Mineralogy, Mineralogical Society of America, 12*, 644 p.

Roedder, E. & Bodnar, R.J. 1980. Geologic Pressure Determinations from Fluid Inclusion Studies. *Annual Review of Earth and Planetary Sciences, 8*: 263-301. https://www.researchgate.net/deref/http%3a%2f%2fdx.doi.org%2f10.1146%2fannurev.ea.08.050180.001403

Sheppard, S. 1986. Characterization and isotopic variations in natural waters. *In:* VALLEY, J.; TAYLOR JR., H. & O'NEILL, J. (Eds.). Stable isotopes in high temperature geological processes. *Reviews in Mineralogy, Mineralogical Society of America, 16*: 165-184.

Suzuoki, T. & Epstein, S. 1976. Hydrogen isotope fractionation between OH-bearing minerals and water. *Geochimica et Cosmochimica Acta, 40*: 1229-1240. https://www.sciencedirect.com/science/article/pii/0016703776901587

Zheng, Y.F. 1996. Oxygen isotope fractionations involving apatites: Application to paleotemperature determination. *Chemical Geology, 127*: 177-187. https://www.sciencedirect.com/science/article/pii/0009254195000887

Zhang, L.G.; Liu; J.X. & Chen, Z.S. 1989. Oxigen isotope fractionation in the quartz-water-salt system. *Economic Geology, 84(6)*: 1643-1650. https://doi.org/10.2113/gsecongeo.84.6.1643

Zhang, L.G.; Liu, J.X.; Chen, Z.S. & Zhou, H.B. 1994. Experimental investigations of oxygen isotope fractionation in cassiterite and wolframite. *Economic Geology, 89(1)*: 150-157. https://doi.org/10.2113/gsecongeo.89.1.150

Received: 27 June 2020

Accepted: 15 December 2020

How to cite:

González Chiozza, S. 2021. Origin and Evolution of the W mineralization in the Intrusion-related Hydrothermal Deposits of the Cerro Áspero Mining District, Sierras Pampeanas, Argentina. *Anuário do Instituto de Geociências, 44*: 35969. DOI 1982-3908_2021_44_35969